



HAL
open science

Enhancement of Sensorless Control for Non-Sinusoidal Multiphase Drives-Part I: Operation in Medium and High-Speed Range

Youssef Mini, Ngac Ky Nguyen, Eric Semail, Duc Tan Vu

► **To cite this version:**

Youssef Mini, Ngac Ky Nguyen, Eric Semail, Duc Tan Vu. Enhancement of Sensorless Control for Non-Sinusoidal Multiphase Drives-Part I: Operation in Medium and High-Speed Range. *Energies*, 2022, 15 (2), pp.607. 10.3390/en15020607 . hal-03553298

HAL Id: hal-03553298

<https://hal.science/hal-03553298v1>

Submitted on 2 Feb 2022

HAL is a multi-disciplinary open access archive for the deposit and dissemination of scientific research documents, whether they are published or not. The documents may come from teaching and research institutions in France or abroad, or from public or private research centers.

L'archive ouverte pluridisciplinaire **HAL**, est destinée au dépôt et à la diffusion de documents scientifiques de niveau recherche, publiés ou non, émanant des établissements d'enseignement et de recherche français ou étrangers, des laboratoires publics ou privés.

Enhancement of Sensorless Control for Non-Sinusoidal Multiphase Drives - Part I: Operation in Medium and High-Speed Range

Youssef Mini ¹, Ngac Ky Nguyen ^{1*}, Eric Semail ¹ and Duc Tan Vu ^{1,2}

¹ Arts et Métiers Institute of Technology, Univ. Lille, Centrale Lille, HEI, HESAM Université, ULR 2697 - L2EP - Laboratoire d'Electrotechnique et d'Electronique de Puissance, F-59000 Lille, France; youssouf.mini@ensam.eu (Y.M.); eric.semail@ensam.eu (E.S.); vductan-tdh@tnut.edu.vn (D.T.V.)

² Faculty of Electrical Engineering, Thai Nguyen University of Technology, No. 666, 3-2 Street, Thai Nguyen 250000, Vietnam

* Correspondance : ngacky.nguyen@ensam.eu (N.K.N.)

Abstract: This two-part study proposes a new sensorless control strategy for non-sinusoidal multiphase permanent magnet synchronous machines (PMSMs), especially in integrated motor drives (IMDs). Based on the Sliding Mode Observer (SMO), the proposed sensorless control strategy uses the signals (currents and voltages) of all fictitious machines of the multiphase PMSMs. It can estimate the high-accuracy rotor position that is required in the vector control. This proposed strategy is compared to the conventional sensorless control strategy applying only current and voltage signals of the main fictitious machine, including the fundamental component of back electromotive force (back-EMF) of the non-sinusoidal multiphase PMSMs. Therefore, in order to choose an appropriate sensorless control strategy for the non-sinusoidal multiphase PMSMs, these two sensorless control strategies will be highlighted in terms of precision in the rotor position and speed estimations. Simulation and experimental results of a non-sinusoidal seven-phase PMSM will be shown to verify and compare the two sensorless control strategies. In this part of the study (part I), only the sensorless control in medium and high-speed range is considered. The sensorless control at zero and low-speed range will be treated in the second part of this study (part II).

Keywords: Sensorless control; back-EMF observer; sliding mode observer; integrated motor drive; multiphase machine; seven-phase permanent magnet synchronous machine.

1. Introduction

With the huge development of electrified automotive vehicles, low-cost electrical drives but with high performances are sought. At first, for a good torque quality in terms of low ripples and high dynamics, vector control with precise knowledge of rotor position is a requirement. With three-phase PMSM, it is then necessary to consider machines with sinusoidal electromotive forces. This requirement impacts their cost and torque density in comparison with three-phase machine with trapezoidal electromotive forces. With n -phase multiphase PMSM, it is possible to obtain simultaneously the torque quality of a three-phase sinusoidal PM machines and the torque density [1, 2] of non-sinusoidal trapezoidal three-phase PM machines thanks to their specific harmonic properties. More precisely, for a machine with $(2k+1)$ phases, a generalized vector control with k dq rotating frames using k rotation angles has been proposed [3, 4] in case of electromotive force spectrum with $(k+1)$ harmonics. These multiphase machines not only place less stress on design and manufacturing, they also exhibit tolerance to power failures. Moreover, the usual drawback of numerous $(2k+1)$ AC cables to connect between the machine and an external Voltage Source Inverter is disappearing with the development of integrated

motor drives (IMDs) in which the power inverter is integrated into the electrical machine [5-7].

In this context, the mechanical position encoder appears to be the weak point with its constraints of size, cost and reliability leading to the development of a “soft” position sensor, i. e., applying only electrical sensors (of currents and voltages) or integrated magnetic sensors (Hall effect sensors). As sensorless controls have been extensively studied for three-phase machines the first approach is to consider the methods already developed to estimate the position keeping in mind nevertheless that for a non-sinusoidal machine with $(2k+1)$ phases it is necessary to consider not only one rotation angle but k in order to work in k (d-q) rotating frames. Each rotating angle is chosen in relation to the most important harmonic component of the electromotive force at the origin of torque in the corresponding fictitious machine [3, 4, 8]. As example for a five-phase machine θ (resp 3θ) for the first (resp. the second) fictitious machine associated to the first (resp. the third) harmonic.

For three-phase machines, there have been several methods which have proposed the sensorless control strategies of PMSM [9, 10]. All methods are based on the measurement of currents and voltages of the machines to compute (estimate) the rotor position and speed information. As back-EMFs are functions of the rotor position, they can be used to provide the rotor position and speed information [11]. Based on the machine model, the quality of the back-EMF estimation essentially depends on their amplitude. It means that when the machine operates at low speed, the estimation will be not precise because of the low amplitude of back-EMFs [11]. Indeed, in the sensorless control, back-EMFs are estimated from current and voltage signals, and the voltage amplitude is very tiny at low speed, especially for low-voltage machines. In addition, the voltage signal is affected by the voltage drop in inverter legs and disturbed by the non-linearities of the inverter and PWM harmonics [12]. When the rotating speed decreases, the signal-to-noise ratio is reduced, leading to a noisier estimation of rotor position and speed. When the machine runs at a significant speed, the back-EMF estimation becomes more precise, allowing an accurate estimation of the rotor position [12]. In fact, for the sensorless control of PMSM, two speed range have been defined in the literature review [12, 13] according to the rotor speed. The “medium and high-speed range” refers to speeds greater than 10% of the base speed while the “zero and low-speed range” includes speeds less than 10% of the base speed.

In zero and low-speed range, the sensorless control of PMSM is based on High Frequency (HF) signal injection methods [14, 15]. The basic theory of these methods is based on the tracking of machine saliency (inductance variations due to geometrical effects and saturation) that is modulated by the rotor position [16]. Meanwhile, the sensorless control in medium and high-speed range, which will be treated in this paper, is essentially based on back-EMF observers to estimate the rotor position information [9, 17]. These observers are almost based on techniques such as Luenberger Observer (LO) [18], Model Reference Adaptive System (MRAS) [19], Extended Kalman Filter (EKF) [20], and SMO [21]. However, all these techniques are not feasible at standstill and low speed with the very low amplitude of back-EMF. Among these techniques, the SMO has been widely used for the sensorless control of PMSM since the chattering phenomenon (main disadvantage of SMO) can be reduced by using the sigmoid function as non-linear element [21, 22] or the novel hybrid reaching law with disturbance observer as proposed in [23]. The sigmoid function is used by SMO to correct the error between the estimated variables and the measured ones. This structure can maintain a good robustness of the entire observer to perturbations [21]. Therefore, to perform the accurate sensorless control of non-sinusoidal multiphase PMSMs, SMO is preferable due to its simple implementation compared to EKF. Indeed, EKF requires a long calculation time especially in the case of multiphase machines [24]. Moreover, compared to the LO [25] and MRAS [26], SMO [27] presents a robust structure dealing with variations of machine parameters and noises.

Non-sinusoidal multiphase PMSMs presents non-sinusoidal back-EMF signals. It means that the torque of the multiphase PMSMs is produced not only by the fundamental of back-EMFs and currents, but also by the other harmonics contained in the back-EMF signal. According to the decomposition theory [28], a real multiphase machine can be decomposed into several fictitious machines (reference frames), including the main fictitious machine (which generates most of the torque) and other fictitious machines. A given family of harmonics is associated with each fictitious machine. Moreover, the sensorless control based on SMO estimates back-EMFs through current and voltage signals, and then deduces the rotor position and speed. Sensorless control strategies for the non-sinusoidal multiphase PMSMs, based on only the fundamental component of back-EMFs (associated with the main fictitious machine), have been found in [27, 29, 30]. In this case, only currents and voltages of the main fictitious machine are used to estimate the rotor position.

In this part of the study, an original sensorless strategy using several harmonics of back-EMFs to estimate an accurate rotor position of non-sinusoidal multiphase machines is proposed. Signals from all fictitious machines (currents and voltages) are required to perform the sensorless control strategy. This is in order to improve the quality of currents regulation of equivalent fictitious machines, that can lead therefore to a good torque response specially in transient states. This proposed strategy is compared with the classical strategy which utilizes only the fundamental component of back-EMF. Both strategies are tested, through simulations, on a non-sinusoidal seven-phase PMSM and a non-sinusoidal five-phase PMSM. The torque of the seven-phase PMSM is mainly produced by the 1st harmonic of back-EMF and current. Meanwhile, the torque of the five-phase PMSM used in this study is mainly generated by the 3rd harmonic of back-EMF and current. The use of different harmonics in this study to generate torque aims at highlighting the generality of the proposed sensorless control strategy to all non-sinusoidal multiphase PMSMs. For advanced verification, both sensorless control strategies will be experimentally verified on a non-sinusoidal seven-phase PMSM. This study is an extension of [31] which has presented only numerical results of seven-phase machines. Compared to [31], more comparisons and experimental results are provided in this present paper. In addition, artificial intelligence is added to solve the multi-harmonic problem of back-EMF.

Part I of this study is organized as follows. The seven-phase PMSM modeling is presented in section 2. The sliding mode observer design and the two sensorless control strategies will be explained and detailed in section 3. Simulation and experimental results will be respectively shown in sections 4 and 5 to analyze and highlight each sensorless control strategy.

2. Seven-phase PMSM Modelling

The design of the non-sinusoidal seven-phase PMSM is proposed in [32] with axial flux machine with one stator and two rotors as shown in Figure 1. It is assumed that there is no magnetic saturation and saliency. The model of the machine in the natural frame can be described in [8] as:

$$\vec{v} = R\vec{i} + [\mathbf{L}]\frac{d\vec{i}}{dt} + \vec{e} \quad (1)$$

where \vec{v} , \vec{e} , and \vec{i} are the 7-dimension vectors of phase voltages, back-EMFs, and phase currents, respectively; $[\mathbf{L}]$ and R are the stator inductance matrix and the stator winding resistance of one phase, respectively.

By using the Concordia matrix [8], a seven-phase PMSM can be decomposed into four fictitious machines. In other words, a real seven-phase PMSM is equivalent to three fictitious two-phase machines and one homopolar machine associated with the different groups of harmonics as shown in Figure 2. Due to a wye connection of stator windings, the homopolar machine is not considered [8].

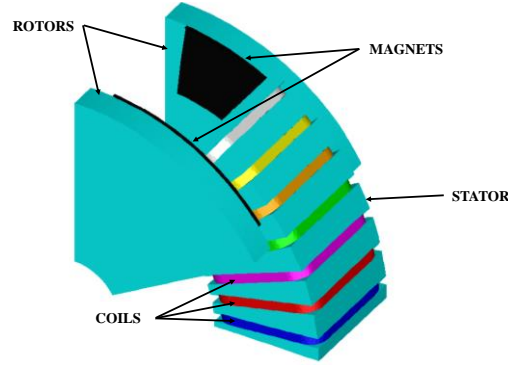


Figure 1. Design of one sixth of the axial flux non-sinusoidal seven-phase PMSM [32].

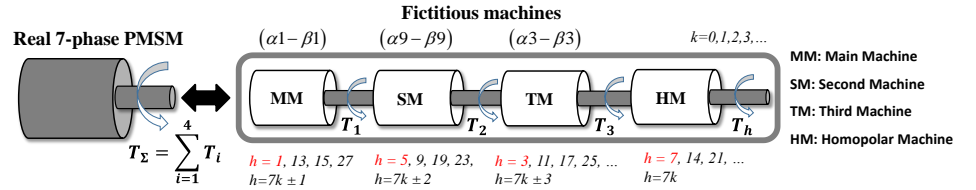


Figure 2. Four fictitious machines and associated harmonic groups of seven-phase PMSM [33].

The measured back-EMF of one phase of the non-sinusoidal seven-phase PMSM and the harmonic spectrum are described in Figure 3. It can be seen that the amplitudes of 1st, 9th and 3rd harmonics are highest in the back-EMF. By decomposing the seven-phase PMSM into several fictitious machines (see Figures 2 and 3), the 1st, 13th, 15th, and 27th harmonics are associated with in the Main Machine (MM), the 9th, 19th and 23rd harmonics present in the Secondary Machine (SM), the 3rd, 11th, and 17th harmonics with the Third Machine (TM). By the same way, the 7th and 21st are associated with the Homopolar Machine (HM) (homopolar currents are equal to zero with the wye connection). Therefore, the model of a seven-phase PMSM, considering the 1st harmonic in MM, the 9th harmonic in SM and the 3rd harmonic in TM, can be expressed in the stationary reference frames $(\alpha - \beta)$ by:

$$\begin{cases} L_m \frac{d\vec{i}_{\alpha\beta 1}}{dt} = -R\vec{i}_{\alpha\beta 1} - \vec{e}_{\alpha\beta 1} + \vec{v}_{\alpha\beta 1} \\ L_s \frac{d\vec{i}_{\alpha\beta 9}}{dt} = -R\vec{i}_{\alpha\beta 9} - \vec{e}_{\alpha\beta 9} + \vec{v}_{\alpha\beta 9} \\ L_t \frac{d\vec{i}_{\alpha\beta 3}}{dt} = -R\vec{i}_{\alpha\beta 3} - \vec{e}_{\alpha\beta 3} + \vec{v}_{\alpha\beta 3} \end{cases} \quad (2)$$

where $\vec{i}_{\alpha\beta i} = [i_{\alpha i} \ i_{\beta i}]^T$, $\vec{e}_{\alpha\beta i} = [e_{\alpha i} \ e_{\beta i}]^T$, and $\vec{v}_{\alpha\beta i} = [v_{\alpha i} \ v_{\beta i}]^T$ with $i = \{1, 9, 3\}$, represent respectively the currents, the back-EMF, and the voltages of the fictitious machines; L_m , L_s , and L_t represent respectively the inductances of MM, SM, and TM. In the following sections, it is assumed $L_m = L_1$, $L_s = L_9$, and $L_t = L_3$.

By considering the main harmonics (1st, 3rd, and 9th) of the back-EMF, the electromagnetic torque of the non-sinusoidal seven-phase PMSM can be obtained by the sum of torques from the three fictitious machines as follows:

$$\Gamma = \Gamma_1 + \Gamma_9 + \Gamma_3 \quad (3)$$

$$\text{with } \left\{ \begin{array}{l} \Gamma_1 = \frac{[e_{\alpha 1} \ e_{\beta 1}][i_{\alpha 1} \ i_{\beta 1}]^T}{\Omega} \\ \Gamma_9 = \frac{[e_{\alpha 9} \ e_{\beta 9}][i_{\alpha 9} \ i_{\beta 9}]^T}{\Omega} \\ \Gamma_3 = \frac{[e_{\alpha 3} \ e_{\beta 3}][i_{\alpha 3} \ i_{\beta 3}]^T}{\Omega} \end{array} \right.$$

where Γ_1 is the torque of MM; Γ_9 is the torque of SM; Γ_3 is the torque of TM; Ω is the rotating speed.

When only the 1st, 3rd and 9th harmonics are considered, the back-EMFs in $(\alpha - \beta)$ frames can be expressed as [8]:

$$\left\{ \begin{array}{l} e_{\alpha 1} = \psi_1 \omega_r \sin \theta_m \\ e_{\beta 1} = -\psi_1 \omega_r \cos \theta_m \\ e_{\alpha 9} = \psi_9 \omega_r \sin \theta_s \\ e_{\beta 9} = -\psi_9 \omega_r \cos \theta_s \\ e_{\alpha 3} = \psi_3 \omega_r \sin \theta_t \\ e_{\beta 3} = -\psi_3 \omega_r \cos \theta_t \end{array} \right. \quad (4)$$

where ψ_1 , ψ_3 , and ψ_9 are the 1st, 3rd, and 9th harmonics of the flux linkage of the permanent magnets, respectively; ω_r is the electrical angular velocity; θ_m , θ_s , and θ_t represent respectively the electrical rotation angles of the fictitious MM, SM, and TM.

To perform an accurate vector control, the rotor position information is required to compute the Park transformation in the rotor reference frames $(d - q)$. In this context, from (4), the back-EMF signal contains the rotor position information. Thus, to implement the sensorless control of the seven-phase PMSM, an algorithm based on the SMO will be designed to estimate the back-EMF signals which are necessary to extract the rotor position and speed information with high accuracy.

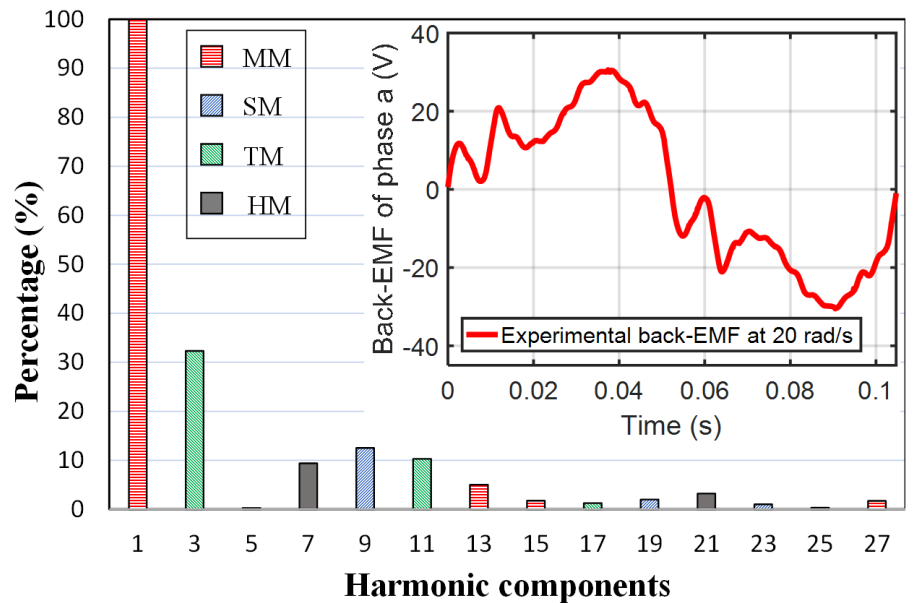


Figure 3. Waveform and harmonic spectrum of the experimental back-EMF of phase “a” at 20 rad/s [34].

This machine, with 32% for the third harmonic and 12% for the ninth harmonic, is interesting to compare the two approaches that will be presented in this article. These approaches are to estimate the three rotation angles which are used for the determination of the three rotating frames in a seven-phase machine.

3. Sliding Mode Observer – based Sensorless Control Strategies

The SMO algorithm can be designed in $(\alpha - \beta)$ frames. Measured currents and reference voltages are used as inputs of the numerical algorithm [22] as shown in Figure 4. From the reference voltages and the outputs of the non-linear element (sigmoid function), the currents are estimated in $(\alpha - \beta)$ frame. Then, the estimated currents are compared to the measured currents. The error between these currents is put in the sigmoid function in order to minimize the error. The back-EMF estimation unit is fed by the outputs of the sigmoid function, which contain the back-EMF signal disturbed by a high-frequency component from the chattering phenomenon. The objective is to eliminate the high-frequency component to extract the estimated back-EMF signal for the estimation of the rotor position and speed. The estimation process by SMO is described in Figure 4 for each fictitious machine.

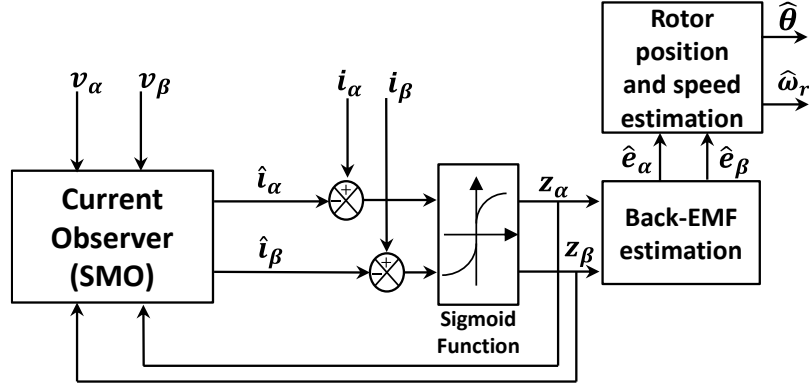


Figure 4. Block diagram of SMO for the sensorless control.

where (v_α, v_β) and (i_α, i_β) are respectively voltages and currents in stationary reference frame $(\alpha - \beta)$; $(\hat{e}_\alpha, \hat{e}_\beta)$ and $(\hat{i}_\alpha, \hat{i}_\beta)$ represent the estimated back-EMF and currents, respectively.

The speed $\hat{\omega}_r$ and rotor position $\hat{\theta}$ are extracted from the estimated back-EMF $(\hat{e}_\alpha, \hat{e}_\beta)$ [22, 27]. The sigmoid function, used to reduce the chattering phenomenon (including a high frequency component) in SMO, is a continuous function [22].

For the seven-phase PMSM, the estimated currents of each fictitious machine by SMO can be expressed as [22]:

$$L_i \left(\frac{d\vec{\hat{i}}_{\alpha\beta i}}{dt} \right) = -R\vec{\hat{i}}_{\alpha\beta i} + \vec{v}_{\alpha\beta i} - k_i F(\vec{\hat{i}}_{\alpha\beta i} - \vec{i}_{\alpha\beta i}) \quad (5)$$

with $F(x)$ is the sigmoid function [22] and:

$$\begin{cases} z_{\alpha i} = k_i F(\hat{i}_{\alpha i} - i_{\alpha i}) \\ z_{\beta i} = k_i F(\hat{i}_{\beta i} - i_{\beta i}) \end{cases} \quad (6)$$

where $i = \{1, 9, 3\}$, and (k_1, k_9, k_3) represent the current observer gains.

By comparing equations (2) and (5), it can be considered that (6) represents respectively the back-EMF signals of MM, SM and TM. However, it should be noted that the signals contain a high-frequency component caused by the sigmoid function "chattering phenomenon". Thus, to extract only the useful back-EMF signals for the rotor position estimation, a back-EMF observer will be constructed. Therefore, based on (6) and (4), the back-EMF observer of each fictitious machine of the seven-phase PMSM is built as [22, 27]:

$$\begin{cases} \frac{d\hat{e}_{\alpha i}}{dt} = -i\hat{\omega}_r \hat{e}_{\beta i} - l_i(\hat{e}_{\alpha i} - z_{\alpha i}) \\ \frac{d\hat{e}_{\beta i}}{dt} = i\hat{\omega}_r \hat{e}_{\alpha i} - l_i(\hat{e}_{\beta i} - z_{\beta i}) \end{cases} \quad (7)$$

where $\vec{\hat{e}}_{\alpha\beta i} = [\hat{e}_{\alpha i} \ \hat{e}_{\beta i}]^T$ is the estimated back-EMF in $(\alpha - \beta)$ frames of the fictitious machines; (l_1, l_9, l_3) represent the SMO gains. The suitable gains (k_1, k_9, k_3) and (l_1, l_9, l_3) , are defined by considering the SMO stability [22]-[27].

As mentioned in section 1, two SMO – based sensorless control strategies for the non-sinusoidal seven-phase PMSM will be detailed and then compared in the next subsections. From the back-EMF estimation in (7), the two strategies can be defined. Specifically, the first strategy (conventional strategy), denoted by S1, uses only the estimated back-EMF signals of fictitious MM (1st harmonic). The second strategy (proposed strategy), denoted by S2, is based on all estimated back-EMF signals (1st, 3rd, and 9th harmonics).

3.1. Conventional Sensorless Control of Seven-phase PMSM using only Main Fictitious Machine (S1)

For this sensorless control strategy, SMO algorithm uses only the fictitious MM signals. By considering only the 1st harmonic in MM, the rotation angle θ_m is assumed as θ . Similarly, with only the 9th and 3rd harmonics in SM and TM, the rotation angles θ_s and θ_t can be obtained directly by multiplying angle θ by 9 (to form 9θ) and 3 (to have 3θ). Because there is no initial phase shift angles in the back-EMF harmonics for this seven-phase PMSM. In fact, the rotor position $\hat{\theta}$ is estimated from MM. After that, angles $3\hat{\theta}$ and $9\hat{\theta}$ are calculated from the multiplications of $\hat{\theta}$ with 3 and 9, respectively. As aforementioned, these angular values are necessary to perform the vector control of SM and TM.

Based on (4) and the relationship between the rotor position and the back-EMF, the estimated values of the rotating speed and rotor position can be written by:

$$\hat{\omega}_r = \frac{\sqrt{\hat{e}_{\alpha 1}^2 + \hat{e}_{\beta 1}^2}}{\psi_1} \quad (8)$$

$$\hat{\theta} = -\arctan\left(\frac{\hat{e}_{\alpha 1}}{\hat{e}_{\beta 1}}\right) \quad (9)$$

From (9) and Figure 5, angles $9\hat{\theta}$ and $3\hat{\theta}$ can be expressed as:

$$9\hat{\theta} = 9(\theta - \theta_{err}) \Rightarrow 9\hat{\theta} = 9\theta - 9\theta_{err} \quad (10)$$

$$3\hat{\theta} = 3(\theta - \theta_{err}) \Rightarrow 3\hat{\theta} = 3\theta - 3\theta_{err} \quad (11)$$

It can be seen from (10) and (11) that the multiplications of $\hat{\theta}$ with 3 and 9 to respectively construct $3\hat{\theta}$ and $9\hat{\theta}$ significantly increase the estimation error. Indeed, the

estimated angle to control fictitious TM will contain an error 3 times bigger than θ_{err} (the error of the estimation process of $\hat{\theta}$ with MM signals). Similarly, the estimation error with $9\hat{\theta}$ to control SM will be 9 times bigger than θ_{err} . Thus, the current regulation of TM and SM will be affected by the estimation error values during the calculations to find the rotor position. It should be noted that such calculations lead to inaccurate and inefficient sensorless control, especially when θ_{err} is high.

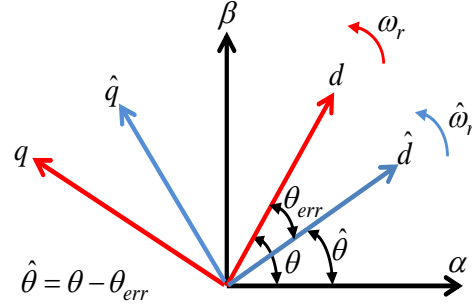


Figure 5. Relationship between the actual $(d-q)$ frame and the estimated $(\hat{d}-\hat{q})$ frame.

3.2. Proposed Sensorless Control of Seven-phase PMSM using all Fictitious Machines (S2)

The proposed SMO – based sensorless control strategy is described in Figure 6. The voltage and current signals (of all fictitious machines) are used for the SMO algorithm as inputs. This is to separately estimate $\hat{\theta}_m$ from MM signals, $\hat{\theta}_s$ from SM signals, and $\hat{\theta}_t$ from TM signals. For this sensorless control strategy, the estimated angles $\hat{\theta}$, 9θ , and 3θ represent respectively angles $\hat{\theta}_m$, $\hat{\theta}_s$, and $\hat{\theta}_t$. Unlike **S1**, angles 9θ and 3θ in **S2** are separately estimated and they do not depend on $\hat{\theta}$ (estimated from fictitious MM signals).

The purpose of this proposed strategy is to avoid the increase of θ_{err} in the estimation of angles θ_s and θ_t due to the multiplications by 9 and 3 as presented in strategy **S1**. Indeed, the estimation of these angles by the back-EMF signals of SM and TM is proposed to increase their estimation quality. In addition, it is assumed that angles θ_m , θ_s , and θ_t contain respectively the offsets θ_{0m} , θ_{0s} , and θ_{0t} , the multiplication of $\hat{\theta}_m$ by 9 and 3 does not allow to obtain the real angles $\hat{\theta}_s$ and $\hat{\theta}_t$. Therefore, each angles should be estimated from corresponding back-EMF signals, as proposed in strategy **S2**, in order to estimate angles θ_s , and θ_t with matching offsets θ_{0s} , and θ_{0t} .

Based on (4), the estimations of rotor position $\hat{\theta}$ and speed $\hat{\omega}_r$ are given by (8) and (9). For the other angles 9θ and 3θ , the estimation can be expressed as:

$$9\theta = -\arctan\left(\frac{\hat{e}_{\alpha 9}}{\hat{e}_{\beta 9}}\right) \quad (12)$$

$$3\theta = -\arctan\left(\frac{\hat{e}_{\alpha 3}}{\hat{e}_{\beta 3}}\right) \quad (13)$$

In the following section, these two SMO – based sensorless control strategies **S1** and **S2** will be tested on a non-sinusoidal seven-phase PMSM and a highly non-sinusoidal five-phase PMSM through numerical simulations in MATLAB/Simulink. In section 5, strategies **S1** and **S2** will be experimentally tested on the non-sinusoidal seven-phase PMSM. The performance of the machine using an encoder (to provide the rotor position) for the control will be used to validate sensorless control strategies **S1** and **S2**. Thus, the effectiveness of each strategy is highlighted in terms of rotor position estimation accuracy.

4. Verification of Sensorless Control Strategies by Simulation Results

Simulations are implemented to verify the effectiveness of the proposed sensorless control strategy **S2** in comparison with the conventional sensorless control strategy **S1**. These two SMO – based sensorless control strategies are implemented in MATLAB/Simulink, and the PWM frequency is set at 10kHz. A torque control is considered for the seven-phase PMSM as described in Figure 6, with a reference torque of 5Nm. The $i_d = 0$ control strategy is carried out. The machine parameters are provided in Table 2.

Table 1. Sliding mode observer parameters

SMO gains	k_1	k_9	k_3	l_1	l_9	l_3
Values	100	500	400	300	1300	2500

Table 2. Seven-phase PMSMs characteristics

Seven-phase PMSM parameters	Values
Stator Resistance of one phase [Ω]	1.4
Self-inductance of one phase [mH]	14.7
Number of pole pairs	3
Speed-normalized amplitude of 1st harmonic of back-EMF [V/rad/s]	1.2650
Speed-normalized amplitude of 9th harmonic of back-EMF [V/rad/s]	0.1569
Speed-normalized amplitude of 3rd harmonic of back-EMF [V/rad/s]	0.4073
Maximum DC bus voltage [V]	200

For torque control using the sensorless strategies, the rotating speed is not required but it is still estimated to verify the feasibility of the proposed sensorless control strategy in response to variations of the speed. The zero and low-speed range is not considered in this part of the study but it is going to be studied in the second part of this study. In the sensorless control simulations, SMO parameters are provided in Table 1.

In Figure 3, the back-EMF signal is measured at 20 rad/s. In fact, the simulations will be examined for a rotor speed around 20 rad/s (~200 rpm). It should be noted that the base speed of this machine is around 400 rpm, because the DC power supply limit is 200 V. The estimated back-EMF, and then the estimated rotor position and speed will be compared to real results supposed obtained by the “encoder”.

4.1. Sensorless Control by Strategy **S1**

As aforementioned in section 3.1, this sensorless control strategy is based only on the estimated back-EMF of the 1st harmonic. It should be noted that the estimated values of the back-EMF components in $(\alpha - \beta)$ frame are obtained from SMO, and then used to estimate the rotor position and speed, as described in section 3. This means that an accurate estimation of the back-EMF signals is necessary for a precise rotor position and speed estimation. In fact, the actual back-EMF and estimated one from SMO for the fictitious MM are shown and compared in Figure 7.

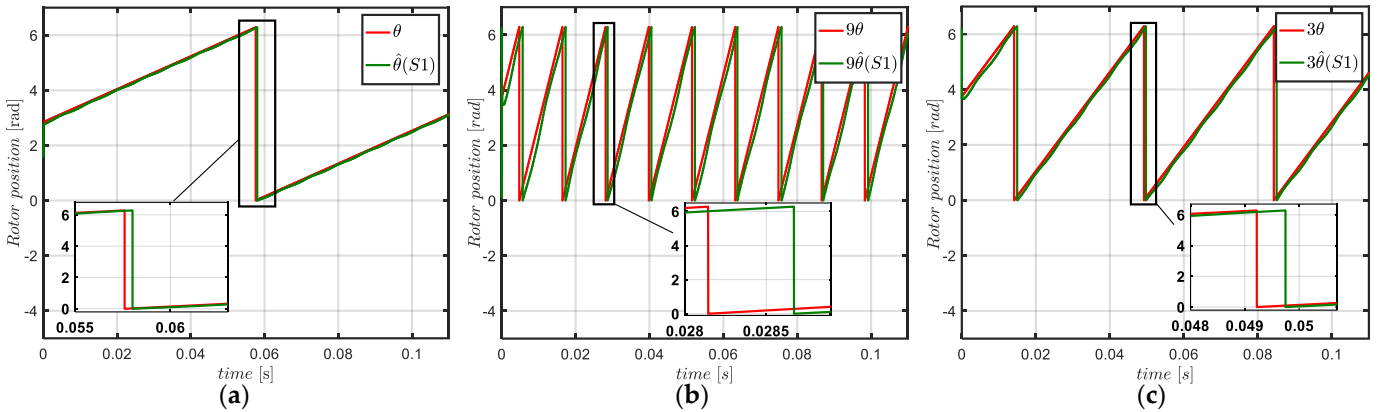


Figure 8. Simulation waveforms of actual and estimated rotor position through (S1): (a) angle required to control MM, (b) angle required to control SM, (c) angle required to control TM.

From Figure 7, the estimated back-EMF in α -axis of the 1st harmonic converges to the actual one. It means that the estimated back-EMF signals of MM are quite similar in terms of amplitude and phase to the actual ones. Based on this precise estimation by SMO, the rotor position is estimated directly from (9) and compared to actual one in Figure 8.

In fact, it can be noticed in Figure 8 (a) that the rotation angle $\hat{\theta}$ is estimated accurately by the strategy S1. The estimation of rotation angles ($3\hat{\theta}$ and $9\hat{\theta}$), which estimated by multiplying respectively $\hat{\theta}$ by 3 and 9 as shown in (11) and (10), is not precise compared to the actual ones as can be seen in Figures 8 (b) et (c). This can be potentially due to the multiplying by 3 and 9 the estimation error θ_{err} resulting in the estimation of angle $\hat{\theta}$. To highlight this significant inaccuracy, the error estimation of different rotation angles will be evaluated for strategy S1 in the section 4.3.

4.2. Sensorless Control by Strategy S2

Unlike the strategy S1, this sensorless control strategy guarantees a separation in the rotation angles estimation. Therefore, the back-EMF estimation of 1st, 9th, and 3rd harmonic are required to perform the sensorless control of the seven-phase PMSM. Accurate estimation of different back-EMF signals is primordial for the feasibility of the strategy S2. Thus, the estimated back-EMF of MM, SM, and TM will be compared to measured ones in Figure 9.

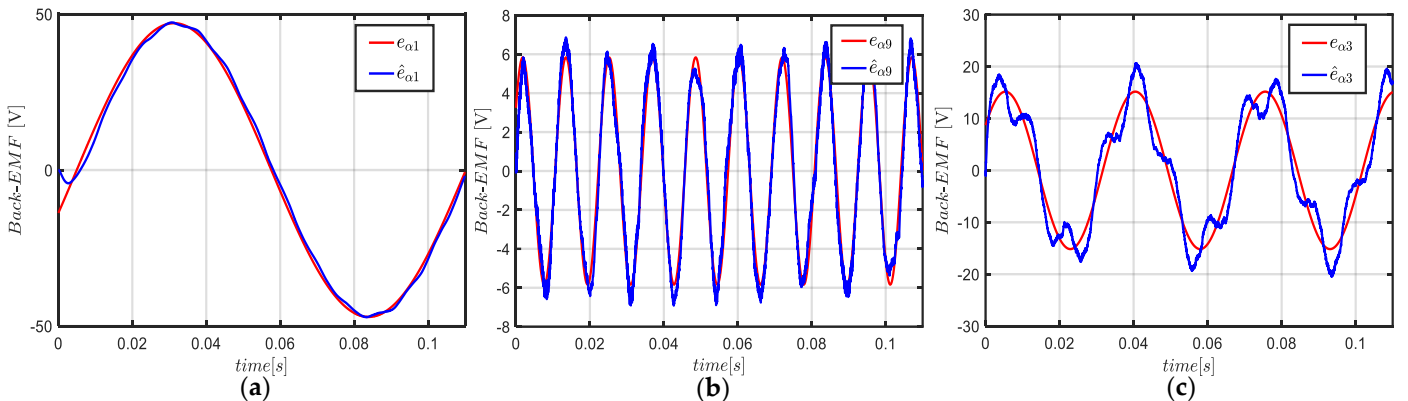


Figure 9. Simulation waveforms of actual and estimated back-EMF in α -axis: (a) the 1st harmonic in MM, (b) the 9th harmonic in SM, (c) the 3rd harmonic in TM.

The back-EMF estimation of 1st harmonic in Figure 9 (a) is the same to the estimated one for strategy S1. As the SMO algorithm used for MM is the same regardless the sensorless control strategy, this back-EMF estimation still accurate compared to the actual one. However, it can be seen in Figures 9 (b) and 9 (c) that the estimated back-EMF of the 9th and 3rd harmonic are disturbed and not accurate compared to actual back-EMF.

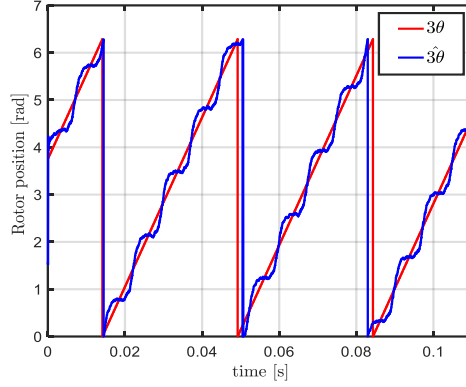


Figure 10. Simulation waveforms: actual rotor position and estimated one through the estimated back-EMF of 3rd harmonic (TM).

This is potentially due to the impact of 19th and 11th harmonics, which are present respectively in SM and TM as shown in Figure 2. It should be noted that the impact of 23rd harmonic in SM and the 17th harmonic in TM does not significant, because of their low amplitudes compared respectively to 9th and 3rd harmonics. In the same way, it can be noticed that the estimated back-EMF signal in TM is more disturbed than the one in SM. This is due to the amplitude of the 11th harmonic which is more important than the 19th harmonic as shown in Figure 3. The impact of such disturbance in the back-EMF estimation signals on the rotor position estimation is evaluated in Figure 10.

Figure 10 shows the actual rotor position and estimated one through the estimated back-EMF of the 3rd harmonic. The estimated rotor position is not precise, impacted by the disturbance on the estimated back-EMF through TM. Therefore, the 9th and 19th harmonics contained in the estimated back-EMF of SM should be separate, in order to extracted only the back-EMF signal of the 9th harmonic. In the same way, the 3rd and 11th harmonics contained in TM should be also separate, in order to extracted only the back-EMF signal of the 3rd harmonic. From the extracted signals, the 9θ and 3θ are directly estimated as shown in (12) and (13), making possible the sensorless control strategy **S2**.

4.2.1. Back-EMF Harmonics Separation

As discussed above, the harmonics contained in the estimated back-EMF of fictitious machines should be separate in order to perform the sensorless control by the strategy **S2**. The separation of 3rd and 11th harmonics contained in the back-EMF of TM will be detailed in the following section, and the same concept will be applied to separate the 9th and 19th contained in the back-EMF of the SM.

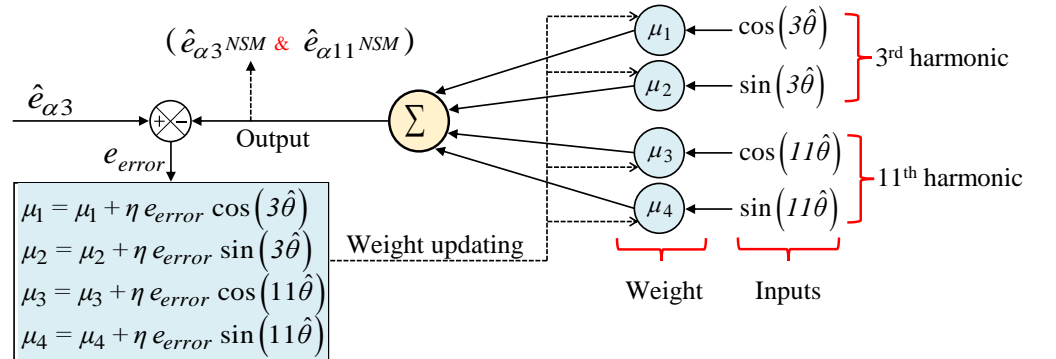


Figure 11: Structure of the ADALINE used by the neural synchronous method [35].

To extract the 3rd harmonic signals from the estimated back-EMF through TM, a neural synchronous method can be used as a relevant solution [36]. The principle of this method is to learn the decomposition of the estimated back-EMF signals in $(\alpha - \beta)$

frame with an Adaline (ADaptive LInear NEuron) [35]. The Adaline neural network represents an intelligent self-learning system that can adapt to achieve a given linear modeling task. In this case, one Adaline per axis is used to learn on-line and estimate each component contained in the estimated back-EMF as shown in Figure 11. The decomposition is therefore learned and it allows to extract the fundamental component (3rd harmonic of the estimated back-EMF through TM) as well as the 11th harmonic. More information about the principle of this neural network (Figure 11) are given in [37].

The Neural Synchronous Method (NSM) will be compared to a traditional method using only a second order Low Pass Filter (LPF). This is in order to separate the 3rd and 11th harmonic by removing, in the estimated back-EMF signals through TM, the 11th harmonic component. Therefore, it can be considered that the signal at the output of the LPF contains only the estimated back-EMF of 3rd harmonic, and that the impact of 11th harmonic is eliminated (filtered). The extracted signal, which contains the 3rd harmonic of estimated back-EMF, will be used to estimate the rotor position 3θ .

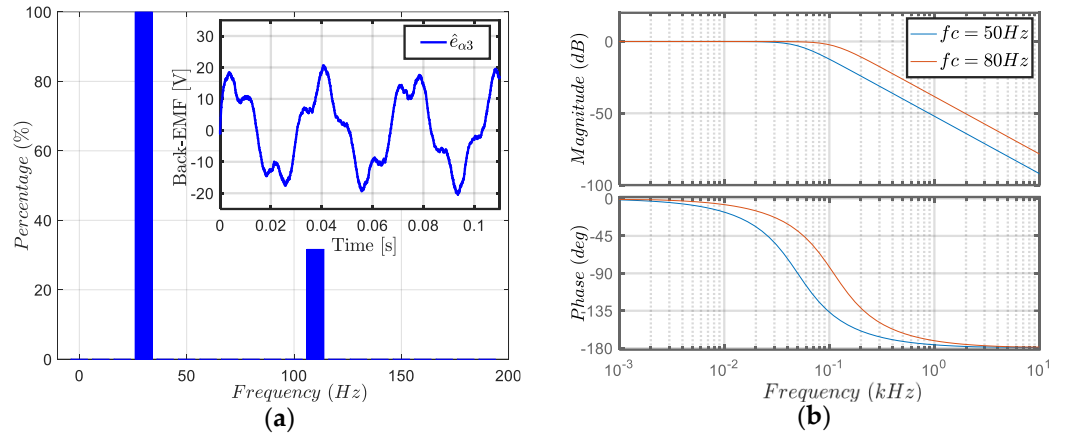


Figure 12. Simulation waveforms: (a) Harmonic spectrum of the estimated back-EMF of 3rd harmonic TM, (b) Bode diagram of the second order Low Pass Filter.

From Figure 12 (a), it can be seen that the estimated back-EMF signal through TM contains the 3rd harmonic at 30 Hz and the 11th harmonic at 110 Hz. As the rotor speed is at 200 rpm, the fundamental of the back-EMF is at 10 Hz. Therefore, the cut off frequency of the second order LPF is set to 50 Hz and then to 80 Hz as shown in Figure. 12 (b), in order to keep the 3rd harmonic (at 30 Hz) and to eliminate the 11th harmonic (at 110 Hz).

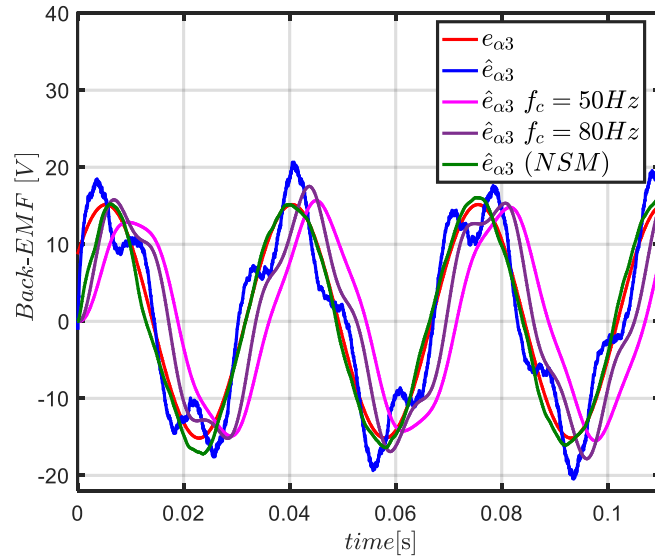


Figure 13. Simulation waveforms of the actual back-EMF of 3rd harmonic and the estimated back-EMF through TM in α -axis using the methods of harmonics separation.

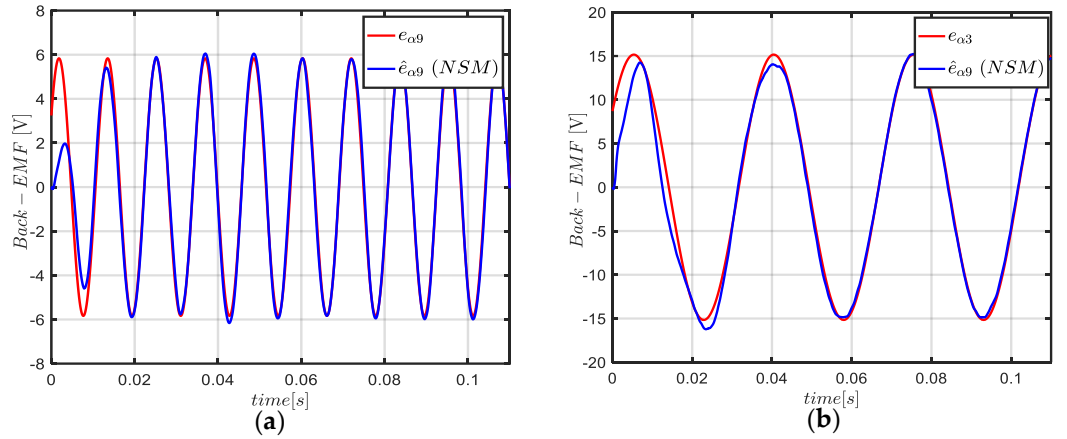


Figure 14. Simulated waveforms of actual and estimated α -axis back-EMF using the neural synchronous method: (a) the 9th harmonic in SM, (b) the 3rd harmonic in TM.

In Figure 13, it can be noticed that the method using a LPF induces an important delay on the estimated back-EMF. For the two cut-off frequency, the resulting signal is out of phase with the actual back-EMF of 3rd harmonic. However, the resulting signal from the neural synchronous method converge with high accuracy to actual back-EMF signal of 3rd harmonic as shown in Figure 13. Therefore, as the harmonics separation method using the NSM is the more accurate, it will be selected to enhance the estimated back-EMF by SMO for the sensorless control strategy **S2**.

In fact, the estimated back-EMF of 3rd harmonic (Figure 14. (b)) is extracted to the estimated one through TM (which contains initially the 3rd and 11th harmonics). In the same way, and applying the neural synchronous method, the estimated back-EMF of 9th harmonic is extracted to the estimated one through SM (which contains initially 9th and 19th harmonics) as shown in Figure 14. (a).

4.2.2. Rotor Position Estimation

We aim by the improvement of the back-EMF estimation process to ensure an accurate estimation of the rotor position and speed by the strategy **S2**. In fact, as described in the section 3.2, the rotation angles used to control each fictitious machine are $\hat{\theta}$, 9θ , and 3θ . Therefore, all estimated angles are compared to the actual angles assumed obtained by “encoder” in Figure 15.

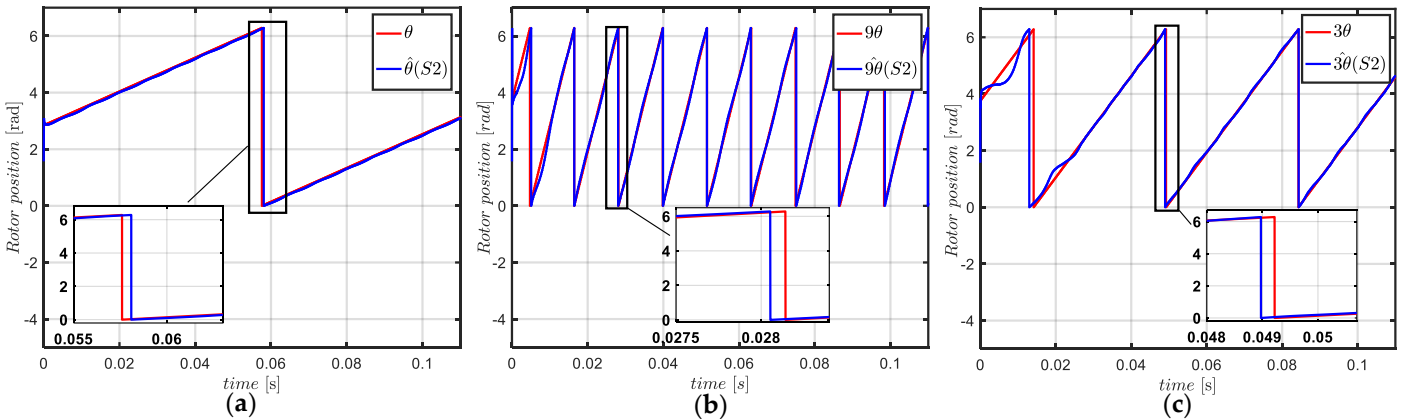


Figure 15. Simulation waveforms of actual and estimated rotor position through (S1) and (S2): (a) angle required to control MM, (b) angle required to control SM, (c) angle required to control TM.

From Figure 15, it can be seen that the estimated rotation angles θ , 9θ , and 3θ converge to the actual ones with accuracy compared to obtained results in Figure 8 with strategy **S1**. In Figure 15 (b), the estimated angle 9θ by strategy **S2** is more precise than

9θ obtained with strategy **S1** in Figure 8 (b). In the same way, Figure 15 (c) shows that the estimated angles 3θ is more precise than the 3θ obtained by the strategy **S1** in Figure 8 (c). Therefore, based on the obtained results for the two sensorless control strategies, it can be already noted that the strategy **S2** is more performant than **S1** in terms of precision especially for the estimated angles required to control the fictitious machines SM and TM. To highlight the performance of strategy **S2**, the estimation error of different rotation angles will be evaluated for strategy **S2**, and then compared to the resulting ones from strategy **S1**.

4.3. Estimation Error Resulting from Strategies S1 and S2

To quantify the estimation errors of the two sensorless control strategies, the errors resulting on the estimated angles will be computed between the actual rotor position and the estimated one. The resulting errors will be compared (Figure 16) for the two strategies, in order to verify the performance of the strategy **S2** observed on Figures 8 and 15.

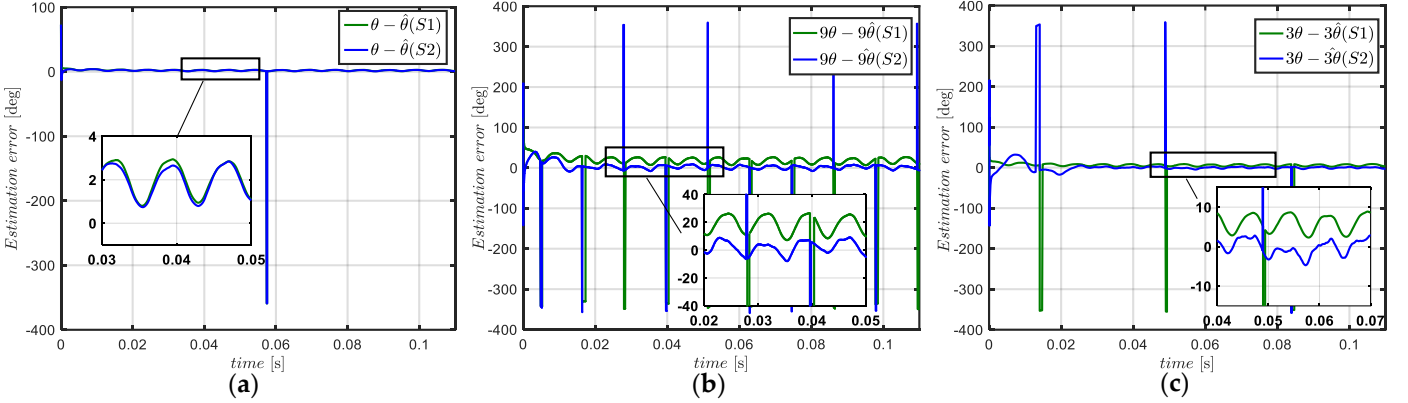


Figure 16. Simulation waveforms of resulting position error (electrical angle) through (**S1**) and (**S2**): (a) error on the angle required to control MM, (b) error on the angle required to control SM, (c) error on the angle required to control TM.

Table 3. Resulting position error (electrical angle) from strategies (**S1**) and (**S2**)

	θ_{err}	θ_{err9}	θ_{err3}
Strategy (S1)	2.3°	20°	7.2°
Strategy (S2)	2.3°	2.5°	2.3°

From Figure 16 (a), it can be seen that the position error resulting of strategies **S1** and **S2** is the same ($\sim 2.3^\circ$). In Figure 16 (b), the position error resulting of the strategy **S1** is around 20° (electrical angle), and the one resulting of the strategy **S2** is around 2.5° (electrical angle). This important position error (20°) is a consequence of the multiplication by 9 the position error θ_{err} as described in section 3.1. In the same way, it can be seen in Figure 16 (c) that the position error resulting of strategy **S1** is around 7.2° , due to the multiplication by 3 the position error θ_{err} . However, the error resulting of strategy **S2** is around 2.3° (electrical angle). These results are summarized in Table 3, with θ_{err9} and θ_{err3} are respectively the position error of rotation angles 9θ and 3θ . Based on the estimation error results, it can be concluded that the sensorless control strategy **S2** is more performant in terms of accuracy than strategy **S1**. In the other hand, the pulses present in the position error (Figure 16), caused by the computation of the estimation error, do not have any impacts on the control loop thanks to the \cos and \sin functions used in the rotating matrix.

The rotor speed is estimated through the estimated back-EMF in $(\alpha - \beta)$ frame as

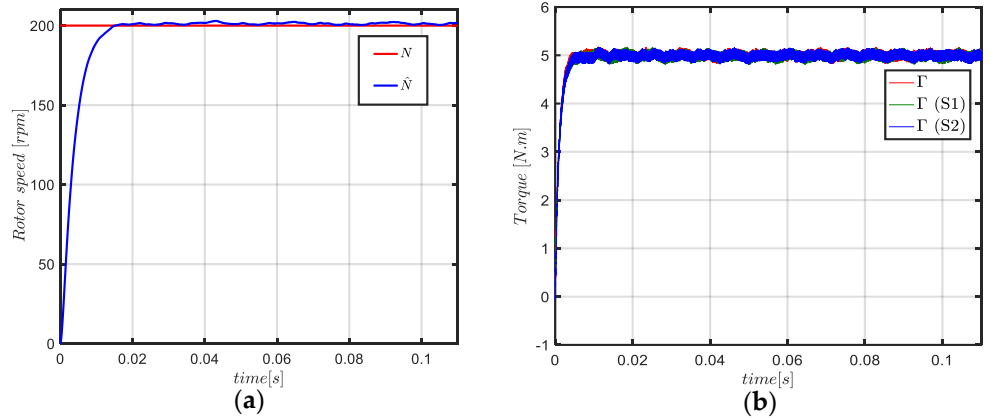


Figure 17. Simulated waveforms: (a) actual and estimated rotor speed, (b) torque when the seven-phase PMSM is controlled by encoder, sensorless control (S1) and sensorless control (S2).

described in (8). It can be noticed that the rotor speed is estimated in the same way (using MM signals) for strategies S1 and S2. As shown in Figure 17 (a), SMO allows an accurate estimation of the rotating speed. In Figure 17 (b), the torque of the seven-phase PMSM resulting of the control with sensor (encoder) and the torque resulting of the sensorless control by strategies S1 and S2 are shown. The two sensorless control strategies guarantee the same quality of torque as the one obtained when the machine is controlled by encoder. It can be noticed that the precision in the estimation of position is higher with S2 strategy (see Table 3). But as the position error around 20° and the one around 7.2° resulting from strategy S1 induces respectively a torque ripples around 13% and 2% of the torques produced by SM and TM, therefore the impact of the position error becomes not significant on the global torque of the seven-phase PMSM. This is due to the small amount of torque produced by SM and TM, compared to the amount of torque produced by the MM. With the machine considered in the next paragraph the impact will be significant.

4.4. Sensorless Control of a Non-sinusoidal Five-phase PMSM

To examine the improvement in terms of torque ripples that can guarantee the proposed sensorless control strategy S2, a highly non-sinusoidal five phase PMSM [38] will be used as mentioned above in section 1. The back-EMF of this machine contains the 1st and 3rd harmonic as shown in Figure 19. The 3rd harmonic represents roughly 120% of the fundamental (1st harmonic). It can be noticed that this high ratio is not classical, but it corresponds to recent studied machines [38-40] which are characterized by a double polarity (p and 3p). In machine for traction this double polarity gives a two-speed gearbox functionality which is interesting when the flux-weakening controls are not satisfying with only one polarity. This concept of multi-polarity with gearbox functionality can be found also in [41, 42] in ISCAD concept for low voltage multiphase induction machines.

This is in order to highlight the sensorless control when the principal amount of torque is not produced by only the fundamental (1st harmonic) of current and back-EMF, as it is by the non-sinusoidal seven-phase PMSM studied above. The modelling of the non-sinusoidal five-phase PMSM and corresponding SMO design are detailed in [43]. The decomposition of the five-phase PMSM to several fictitious machines and the associated harmonics is given by Figure 18.

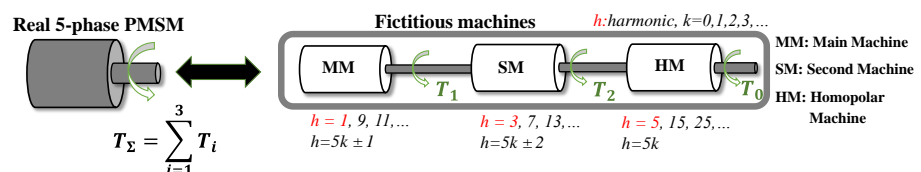


Figure 18. Three fictitious machines and associated groups of harmonics of a five-phase PMSM.

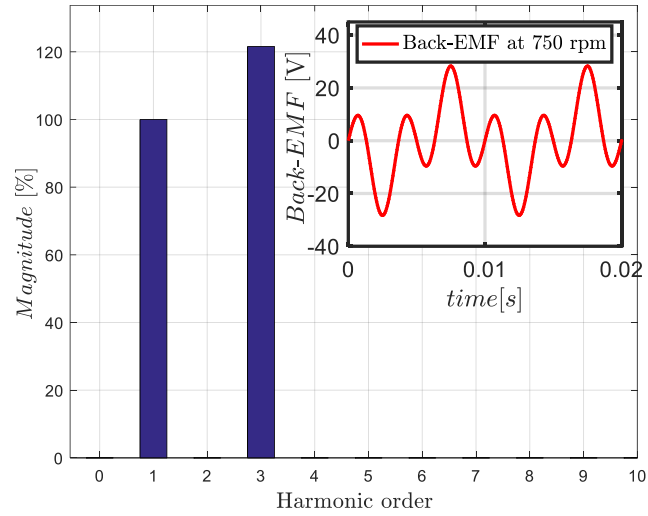


Figure 19. Waveform and harmonic spectrum of the back-EMF of phase “a” of the highly non-sinusoidal five-phase PMSM at 78 rad/s.

As shown in Figure 18, the five-phase PMSM is decomposed to 3 fictitious machines (MM, SM and HM). The torque produced by MM is created by the 1st harmonic, and the torque produced by SM is created by the 3rd harmonic. The fictitious machine HM is not considered with a star connection. For this five-phase machine, the base speed is around 750 rpm for DC power supply limit set at 48 V. To perform the sensorless control of the five-phase PMSM, two rotation angles are required for the vector control: θ_m to control MM, and θ_s to control the SM. Assuming no initial phase shift in the back-EMF harmonics, the rotation angle of 1st harmonic θ_m is considered as θ . In the same way, the rotation angle of the 3rd harmonic θ_s is considered as 3θ . Therefore, the accuracy of the angles estimation by the two sensorless control strategies will be highlighted in the following section.

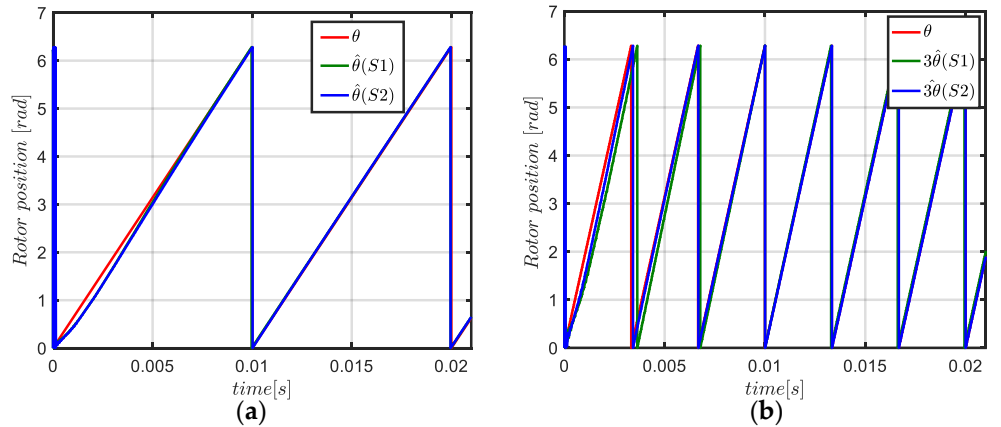


Figure 20. Simulation waveforms at 78 rad/s of actual and estimated rotor position through (S1) and (S2): (a) angle required to control MM, (b) angle required to control SM.

Table 4. Resulting position error (electrical angle) from strategies (S1) and (S2)

	θ_{err}	θ_{err3}
Strategy (S1)	1.5°	5°
Strategy (S2)	1.5°	0.5°

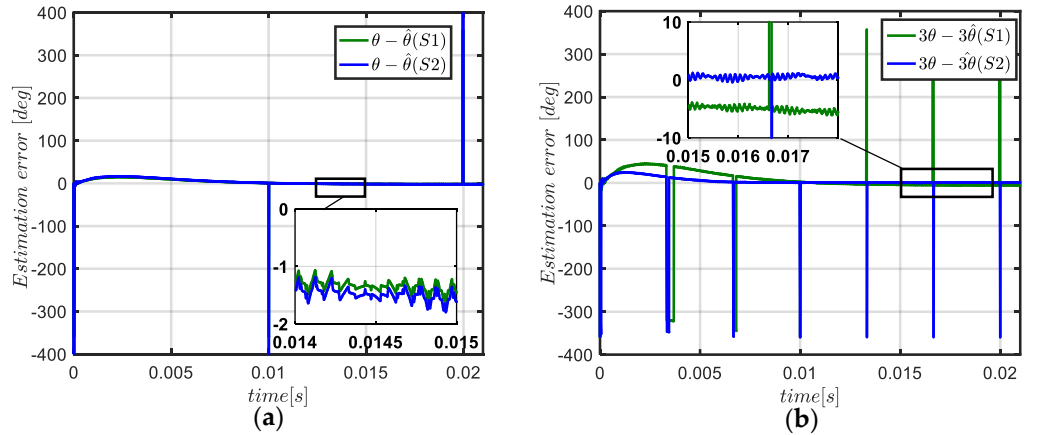


Figure 21. Simulation waveforms at 78 rad/s of resulting position error through (S1) and (S2): (a) error on the angle required to control MM, (b) error on the angle required to control SM.

From the simulation waveforms of Figure 20 (a), the estimated rotor position $\hat{\theta}$ through strategies S1 and S2 converges to the actual one. In this case, the two strategies show the same level of accuracy. This can be verified in Figure 21 (a) which shows that the estimation error resulting from the two strategies is around 1.5° (electrical angle). However, the estimated angle 3θ through the strategy S2 is more accurate than the one estimated through S1 as can be seen in Figure 21 (b). The estimation error resulting from the strategy S1 is around 5° (verifying the theory (11) mentioned above), and the resulting one from S2 is around 0.5° . These results are summarized in Table 4. The impact of the estimation errors on the torque of the highly non-sinusoidal five phase PMSM will be examined in Figure 22.

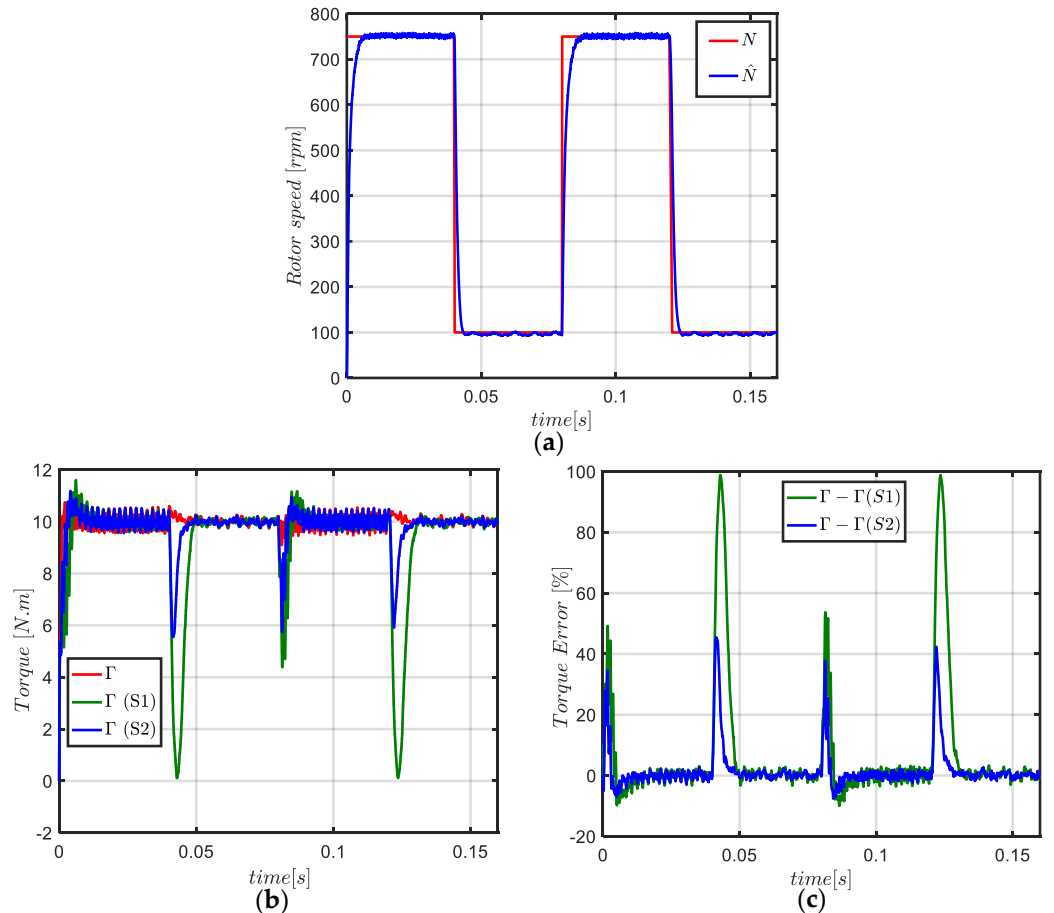


Figure 22. Simulation waveforms for variable rotor speed: torque when the five-phase PMSM is controlled by encoder, sensorless control (S1), and sensorless control (S2).

To highlight the performance of the two sensorless control strategies, the quality of the electromagnetic torque is evaluated when the five phase PMSM operates in steady and transient states. In fact, it can be seen in Figure 22 (a) that the estimated rotor speed converges to the measured one with accuracy in both transient and steady states. For the measured torque in Figure 22 (b), it can be noticed that the two sensorless control strategies guarantee the same quality of torque in the steady states. This can be verified in Figure 22 (c), which shows that the torque error is around 0% of the mean torque for the two strategies at steady states. However, in Figure 22 (b), at transient states (when the rotor speed changes), the torque ripple is more significant when the machine operates under the sensorless control by strategy S1. From Figure 22 (c), the torque error can reach 98% of the mean torque for strategy S1. When the machine operates with the strategy S2, it can be seen that the quality of the torque is much better in the transient states, and the torque error is less than 45% of the mean torque. Thus, the sensorless control strategy S2 is more performant in terms of accuracy and torque ripple than the strategy S1. Therefore, it can be concluded that for non-sinusoidal multiphase PMSMs, producing an important part of torque through SM and TM, the sensorless control should be performed by strategy S2 to avoid a significant torque ripple.

5. Experimental Results

The simulation results showed that the two sensorless control strategies based on the SMO allow an estimation of rotor position, with a significant level of accuracy in the estimation process by the proposed strategy S2. Thus, to further verify the feasibility and the effectiveness of the sensorless control strategies, a test bench constructed by a non-sinusoidal seven-phase PMSM is used.

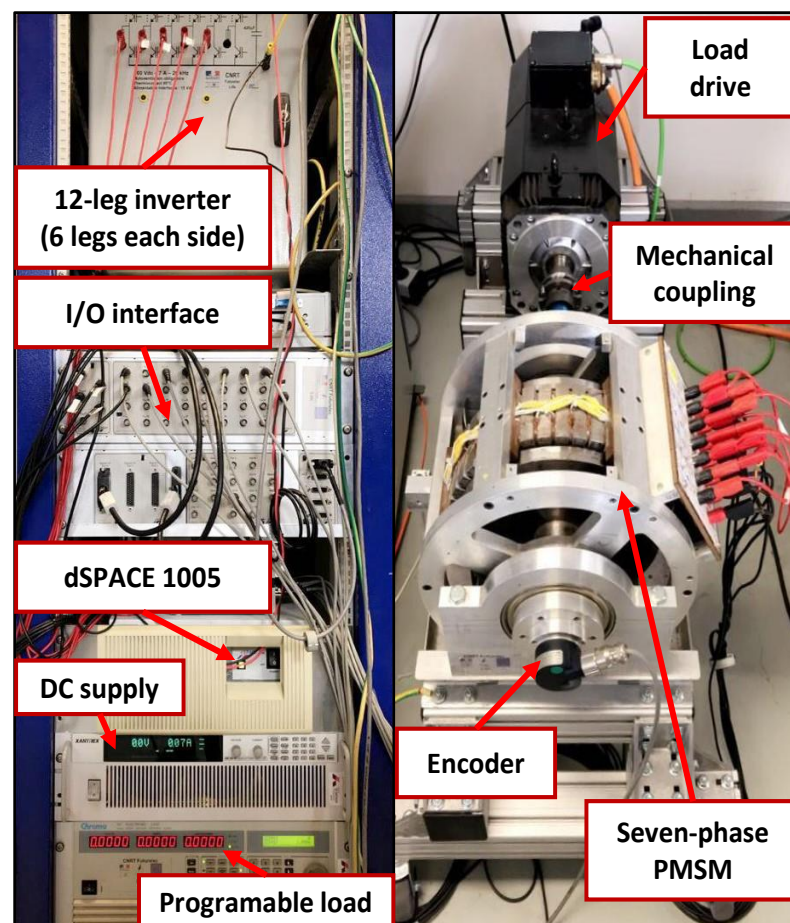


Figure 23. Experimental test bench of the seven-phase PMSM

As shown in Figure 23, the seven-phase PMSM is mechanically coupled to a three-phase PMSM (used as a load drive) which is controlled to tune the speed of the seven-phase machine. We consider a torque control as shown in Figure 6, and the $i_d = 0$ control strategy is carried out. A dSPACE1005 controller is used to drive the seven legs (IGBT) of the inverter supplying the seven-phase PMSM, and to collect the measured data of rotor position and currents. The inverter is supplied by a DC-bus voltage of 200 V. The PWM switching frequency is set to 10 kHz, and the sampling time of the control system is set as 350 μ s. For the measure of the actual rotor position and speed, an incremental encoder is used as shown in Figure 23. Therefore, the control scheme in Figure 6 is implemented experimentally to verify the sensorless control strategies.

5.1. Rotor Position Estimation

From the estimated back-EMF signals, the rotor position is estimated through strategies **S1** and **S2**. For the sensorless control by strategy **S1**, only the estimated back-EMF signals of MM are used to compute the angles $\hat{\theta}$, $9\hat{\theta}$ and $3\hat{\theta}$. And for the sensorless control by Strategy **S2**, all estimated back-EMF signals are used to compute the angles $\hat{\theta}$, 9θ and 3θ required to control respectively the fictitious machines MM, SM and TM. In Figure 24, the measured rotor position "by encoder" is compared to the estimated one, and the resulting estimation errors from strategies **S1** and **S2** are given in Figure 25.

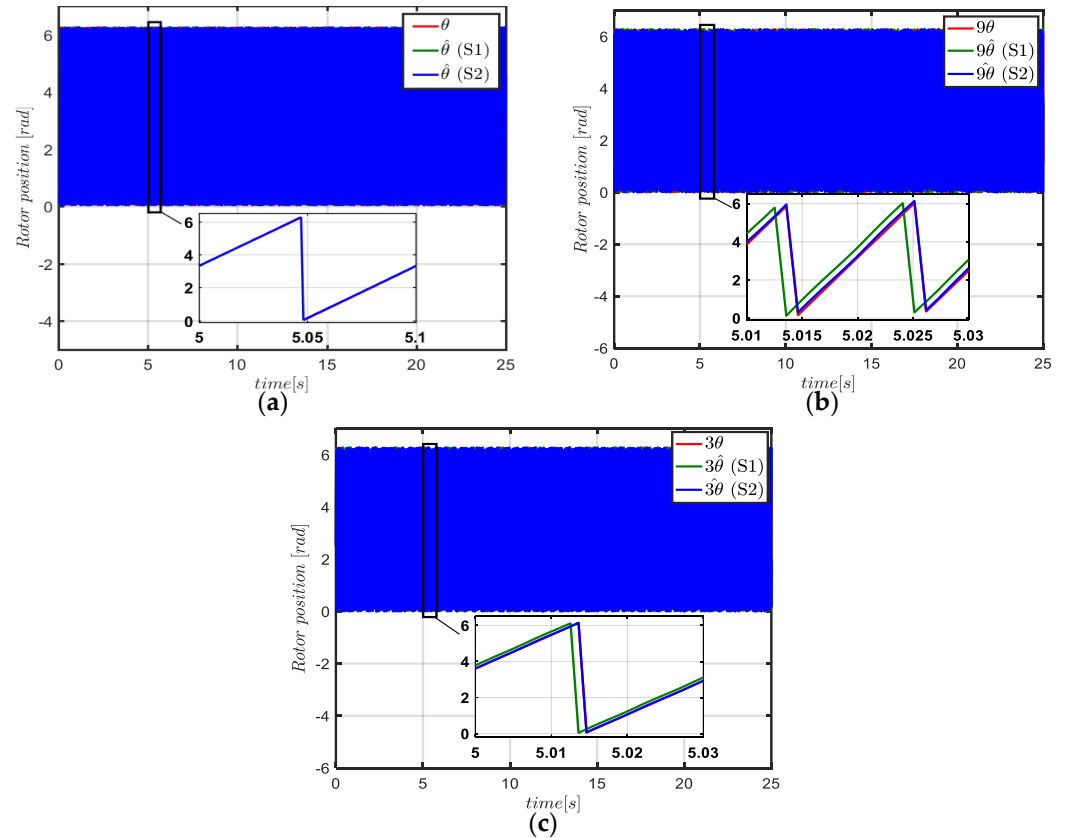


Figure 24. Experimental waveforms: measured and estimated rotor position through (**S1**) and (**S2**): (a) angle required to control MM, (b) angle required to control SM, (c) angle required to control TM.

The experimental waveforms of Figure 24 (a) show that the estimated rotor position $\hat{\theta}$ with strategies **S1** and **S2** converge to the measured one. The position error, resulting to the estimation through the two strategies **S1** and **S2**, is quite similar and around 3.5° as shown in Figure 25 (a). Such error can induce a torque ripples around 0.37% of the produced torque by MM. From Figure 24 (b), it can be noticed that the estimated rotor

position 9θ through strategy **S2** is more precise than the estimated one across strategy **S1**. In Figure 25 (b), the position error, resulting through strategy **S1**, is around 31° (verifying the theory in (10)) due to multiplication by 9 the position error given in Figure 25 (a). However, the position error resulting from strategy **S2** is around 5.7° as shown in Figure 25 (b). Therefore, an error around 31° induces a torque ripples around 32% and the one around 5.7° induces a torque ripples around 0.9% of the produced torque by the SM. In the same way, it can be seen in Figure 24 (c) that the estimated rotor position 3θ is more precise through strategy **S2**. The position error resulting from strategy **S1** is around 11° (inducing a torque ripples around 3.7% of the produced torque by TM), and the one resulting from strategy **S2** is around 2° (inducing a torque ripples around 0.1%) as shown in Figure 25 (c). The position errors results are summarized in Table 5

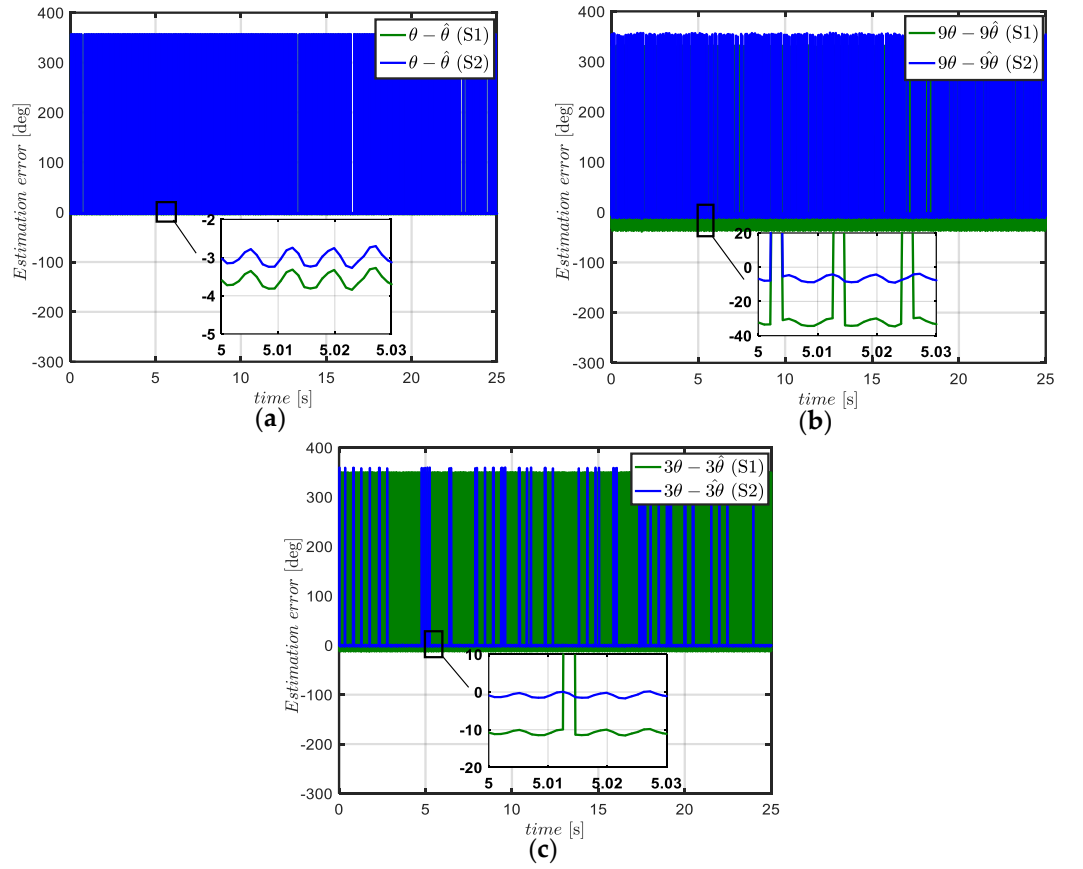


Figure 25. Experimental waveforms: resulting position error through (S1) and (S2): (a) error on the angle required to control MM, (b) error on the angle required to control SM, (c) error on the angle required to control TM.

Table 5. Resulting position error (electrical angle) from strategies (S1) and (S2)

	θ_{err}	θ_{err9}	θ_{err3}
Strategy (S1)	3.5°	31°	11°
Strategy (S2)	3°	5.7°	2°

5.2. Rotor Speed and Electromagnetic Torque

The impact of the estimation errors resulting from the two sensorless control strategies will be highlight when the seven phase PMSM operates at steady and transient states. Therefore, the estimated rotor speed and the measured electromagnetic torque for diffent strategies are given in Figures 26 and 27.

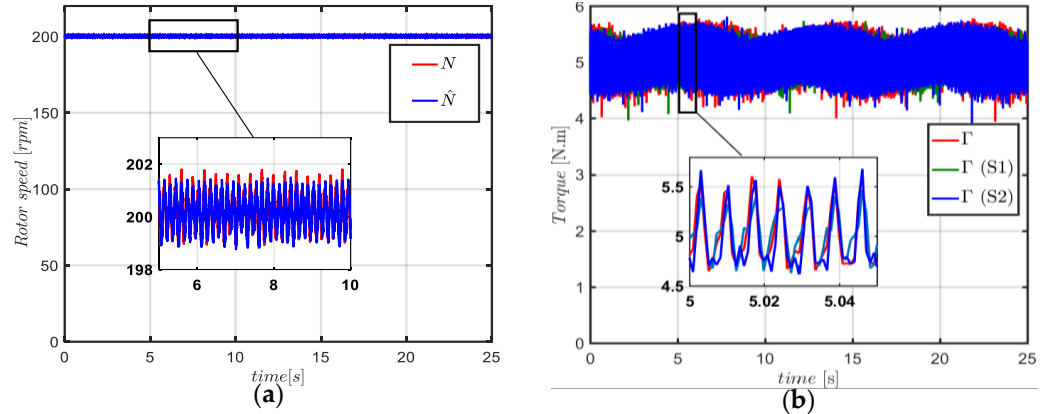


Figure 26. Experimental waveforms: (a) measured and estimated rotor speed, (b) measured torque when the seven-phase PMSM is controlled by encoder, sensorless control (S1) and sensorless control (S2)

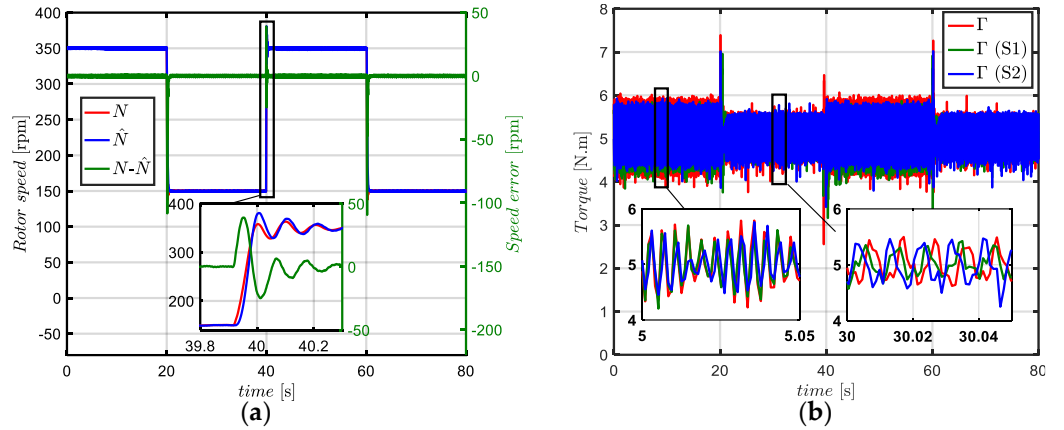


Figure 27. Experimental waveforms for variable rotor speed: (a) measured and estimated rotor speed, (b) measured torque when the seven-phase PMSM is controlled by encoder, sensorless control (S1) and sensorless control (S2)

From the experimental waveforms of Figure 26 (a), the estimated rotor speed by SMO converge to the measured one. When the machine operates at variable speed, SMO ensures this convergence as shown in Figure 27 (a). The estimated rotor speed is computed through the estimated back-EMF signals of MM. In another hand, it can be noticed from Figure 26 (b) and Figure 27 (b) that for the sensorless control by strategy S1 or S2, the measured torque in transient and steady states is similar to the obtained one when the machine is controlled by encoder. This is due, as aforementioned in section 4.3, to the small amount of torque produced by SM and TM of the seven-phase PMSM. Therefore, the estimation errors resulting from the estimation of angles 9θ and 3θ by strategy S1 does not a significant impact on the global torque in this case.

6. Conclusions

In the first part of this study, two sensorless control strategies have been compared through simulation and experimental results. From the results, it can be concluded that SMO can estimate the rotor position with high accuracy (error less than 3°), ensuring a precise sensorless control for non-sinusoidal multiphase PMSMs. For a non-sinusoidal multiphase PMSM in which the torque is mainly produced by the main fictitious machine (MM), strategies S1 (classical) and S2 (proposed) present the same level of accuracy in terms of torque ripples for the sensorless control. However, when the torque is generated by not only MM but also the others fictitious machines (e.g., SM and TM), the proposed sensorless control strategy S2 is more precise to compute the angles for the control of fictitious machines (SM and TM). This allows to perform a more accurate sensorless control

in terms of torque ripples compared to the classical strategy **S1**. This improvement of electromagnetic torque quality (observed for strategy **S2**) is very significant when the machine operates in transient states. However, for steady states, the two sensorless control strategies present a similar performance. In addition, it can be noted that for a non-sinusoidal multiphase PMSM with more than two important harmonics in the same fictitious machine, the sensorless control cannot be performed directly. The separation of harmonics presenting in the fictitious machine is required to estimate accurate back-EMF signals, which are essential to compute the rotor position. Furthermore, the proposed sensorless control strategy **S2** does not require additional hardware to be implemented in the real time since this algorithm is quite similar to the classical strategy **S1**, but the number of observers is multiplied by three.

Author Contributions: Methodology, Software, Validation, Writing—original draft preparation, Y.M.; Writing—review and editing, N.K.N., D.T.V. and E.S; Supervision, N.K.N. and E.S.

Funding: This work has been achieved within the framework of CE2I project. CE2I is co-financed by European Union with the financial support of European Regional Development Fund (ERDF), French State and the French Region of Hauts-de-France.

Conflicts of Interest: The authors declare no conflict of interest.

7. References

1. J. Wang, L. Zhou, and R. Qu, "Harmonic current effect on torque density of a multiphase permanent magnet machine," in *2011 International Conference on Electrical Machines and Systems*, 2011, pp. 1-6.
2. K. Wang, Z. Q. Zhu, and G. Ombach, "Torque Improvement of Five-Phase Surface-Mounted Permanent Magnet Machine Using Third-Order Harmonic," *IEEE Transactions on Energy Conversion*, vol. 29, no. 3, pp. 735-747, 2014.
3. X. Kestelyn and E. SEMAIL, "Vectorial Modeling and Control of Multiphase Machines with Non-salient Poles Supplied by an Inverter," in *Control of Non-conventional Synchronous Motors*, L. Jean-Paul, Ed.: Wiley, 2012, pp. 161-206.
4. M. Slunjski, O. Stiscia, M. Jones, and E. Levi, "General Torque Enhancement Approach for a Nine-Phase Surface PMSM With Built-In Fault Tolerance," *IEEE Transactions on Industrial Electronics*, vol. 68, no. 8, pp. 6412-6423, 2021.
5. Y. Burkhardt, A. Spagnolo, P. Lucas, M. Zavesky, and P. Brockerhoff, "Design and analysis of a highly integrated 9-phase drivetrain for EV applications," in *2014 International Conference on Electrical Machines (ICEM)*, 2014, pp. 450-456.
6. X. Deng, S. Lambert, B. Mecrow, and M. A. S. Mohamed, "Design Consideration of a High-Speed Integrated Permanent Magnet Machine and its Drive System," in *2018 XIII International Conference on Electrical Machines (ICEM)*, 2018, pp. 1465-1470.
7. R. Abebe *et al.*, "Integrated motor drives: state of the art and future trends," *IET Electric Power Applications*, vol. 10, no. 8, pp. 757-771, 2016.
8. F. Locment, E. Semail, and X. Kestelyn, "Vectorial Approach-Based Control of a Seven-Phase Axial Flux Machine Designed for Fault Operation," *IEEE Transactions on Industrial Electronics*, vol. 55, no. 10, pp. 3682-3691, 2008.
9. P. Vas, *Sensorless Vector and Direct Torque Control* Oxford University Press, 1998, pp. 1-729.
10. S. J. Rind, M. Jamil, and A. Amjad, "Electric Motors and Speed Sensorless Control for Electric and Hybrid Electric Vehicles: A Review," in *2018 53rd International Universities Power Engineering Conference (IUPERC)*, 2018, pp. 1-6.
11. L. A. D. S. Ribeiro, M. C. Harke, and R. D. Lorenz, "Dynamic Properties of Back-emf Based Sensorless Drives," in *Conference Record of the 2006 IEEE Industry Applications Conference Forty-First IAS Annual Meeting*, 2006, vol. 4, pp. 2026-2033.
12. R. W. Hejny and R. D. Lorenz, "Evaluating the Practical Low-Speed Limits for Back-EMF Tracking-Based Sensorless Speed Control Using Drive Stiffness as a Key Metric," *IEEE Transactions on Industry Applications*, vol. 47, no. 3, pp. 1337-1343, 2011.
13. G. Bo, S. Doki, T. Furukawa, and N. Minoshima, "The position-sensorless control of low voltage high power permanent magnet synchronous motors in zero/low-speed regions," in *IECON 2016 - 42nd Annual Conference of the IEEE Industrial Electronics Society*, 2016, pp. 2963-2968.
14. G. Liu, C. Geng, and Q. Chen, "Sensorless Control for Five-Phase IPMSM Drives by Injecting HF Square-Wave Voltage Signal into Third Harmonic Space," *IEEE Access*, vol. 8, pp. 69712-69721, 2020.
15. W. Zine *et al.*, "Optimisation of HF signal injection parameters for EV applications based on sensorless IPMSM drives," *IET Electric Power Applications*, vol. 12, no. 3, pp. 347-356, 2018.
16. M. Ramezani and O. Ojo, "The Modeling and Position-Sensorless Estimation Technique for A Nine-Phase Interior Permanent-Magnet Machine Using High-Frequency Injections," *IEEE Transactions on Industry Applications*, vol. 52, no. 2, pp. 1555-1565, 2016.
17. O. Benjak and D. Gerling, "Review of position estimation methods for IPMSM drives without a position sensor part II: Adaptive methods," in *The XIX International Conference on Electrical Machines - ICEM 2010*, 2010, pp. 1-6.
18. A. Andersson and T. Thiringer, "Motion Sensorless IPMSM Control Using Linear Moving Horizon Estimation With Luenberger Observer State Feedback," *IEEE Transactions on Transportation Electrification*, vol. 4, no. 2, pp. 464-473, 2018.

19. Y. Ouvang and Y. Dou, "Speed Sensorless Control of PMSM Based on MRAS Parameter Identification," in *2018 21st International Conference on Electrical Machines and Systems (ICEMS)*, 2018, pp. 1618-1622.
20. Y. Shi, K. Sun, L. Huang, and Y. Li, "Online Identification of Permanent Magnet Flux Based on Extended Kalman Filter for IPMSM Drive With Position Sensorless Control," *IEEE Transactions on Industrial Electronics*, vol. 59, no. 11, pp. 4169-4178, 2012.
21. Z. Qiao, T. Shi, Y. Wang, Y. Yan, C. Xia, and X. He, "New Sliding-Mode Observer for Position Sensorless Control of Permanent-Magnet Synchronous Motor," *IEEE Transactions on Industrial Electronics*, vol. 60, no. 2, pp. 710-719, 2013.
22. J. Yang, M. Dou, and D. Zhao, "Iterative sliding mode observer for sensorless control of five-phase permanent magnet synchronous motor," *Bulletin of the Polish Academy of Sciences Technical Sciences*, vol. 65, no. 6, pp. 845-857, 2017.
23. X. Sun, J. Cao, G. Lei, Y. Guo, and J. Zhu, "A Composite Sliding Mode Control for SPMSM Drives Based on a New Hybrid Reaching Law With Disturbance Compensation," *IEEE Transactions on Transportation Electrification*, vol. 7, no. 3, pp. 1427-1436, 2021.
24. T. Michalski, C. Lopez, A. Garcia, and L. Romeral, "Sensorless control of five phase PMSM based on extended Kalman filter," in *IECON 2016 - 42nd Annual Conference of the IEEE Industrial Electronics Society*, 2016, pp. 2904-2909.
25. C. Olivieri, G. Fabri, and M. Tursini, "Sensorless control of five-phase brushless DC motors," in *2010 First Symposium on Sensorless Control for Electrical Drives*, 2010, pp. 24-31.
26. K. Saad, K. Abdellah, H. Ahmed, and A. Iqbal, "Investigation on SVM-Backstepping sensorless control of five-phase open-end winding induction motor based on model reference adaptive system and parameter estimation," *Engineering Science and Technology, an International Journal*, 2019.
27. L. Zhang, Y. Fan, C. Li, A. Nied, and M. Cheng, "Fault-Tolerant Sensorless Control of a Five-Phase FTFSCW-IPM Motor Based on a Wide-Speed Strong-Robustness Sliding Mode Observer," *IEEE Transactions on Energy Conversion*, vol. 33, no. 1, pp. 87-95, 2018.
28. E. Semail, X. Kestelyn, and A. Bouscayrol, "Right harmonic spectrum for the back-electromotive force of an n-phase synchronous motor," in *Conference Record of the 2004 IEEE Industry Applications Conference, 2004. 39th IAS Annual Meeting.*, 2004, vol. 1, pp. 1-78.
29. H. Chen, C. Hsu, and D. Chang, "Speed control for two series-connected five-phase permanent-magnet synchronous motors without position sensor," in *2016 IEEE 25th International Symposium on Industrial Electronics (ISIE)*, 2016, pp. 198-203.
30. O. Stiscia, M. Slunjski, E. Levi, and A. Cavagnino, "Sensorless Control of a Nine-phase Surface Mounted Permanent Magnet Synchronous Machine with Highly Non-Sinusoidal Back-EMF," in *IECON 2019 - 45th Annual Conference of the IEEE Industrial Electronics Society*, 2019, vol. 1, pp. 1327-1332.
31. Y. Mini, N. K. Nguyen, and E. Semail, "A novel Sensorless Control Strategy Based on Sliding Mode Observer for Non-Sinusoidal Seven-phase PMSM," in *The 10th International Conference on Power Electronics, Machines and Drives (PEMD 2020)*, 2020, vol. 2020, pp. 694-699.
32. F. Locment, E. Semail, X. Kestelyn, and A. Bouscayrol, "Control of a Seven-phase Axial Flux Machine Designed for Fault Operation," in *IECON 2006 - 32nd Annual Conference on IEEE Industrial Electronics*, 2006, pp. 1101-1107.
33. A. B. E. Semail, J.P. Hautier, "Vectorial formalism for analysis and design of polyphase synchronous machines," *European Physical Journal: Applied Physics, EDP Sciences*, pp. 207-220, 2003, 22 (3).
34. D. T. Vu, N. K. Nguyen, E. Semail, and T. J. d. S. Moraes, "Control strategies for non-sinusoidal multiphase PMSM drives in faulty modes under constraints on copper losses and peak phase voltage," *IET Electric Power Applications*, vol. 13, no. 11, pp. 1743-1752, 2019.
35. N. K. Nguyen, D. O. Abdeslam, P. Wira, D. Flieller, and J. Merckle, "Artificial neural networks for harmonic currents identification in active power filtering schemes," in *2008 34th Annual Conference of IEEE Industrial Electronics*, 2008, pp. 2696-2701.
36. D. Flieller, N. K. Nguyen, P. Wira, G. Sturtzer, D. O. Abdeslam, and J. Mercklé, "A Self-Learning Solution for Torque Ripple Reduction for Nonsinusoidal Permanent-Magnet Motor Drives Based on Artificial Neural Networks," *IEEE Transactions on Industrial Electronics*, vol. 61, no. 2, pp. 655-666, 2014.
37. D. T. Vu, N. K. Nguyen, and E. Semail, "Eliminations of Low-frequency Current Harmonics for Five-phase Open-end Winding Non-sinusoidal Machine Drives applying Neural Networks," in *IECON 2020 The 46th Annual Conference of the IEEE Industrial Electronics Society*, 2020, pp. 4839-4844.
38. B. Aslan and E. Semail, "New 5-phase concentrated winding machine with bi-harmonic rotor for automotive application," in *2014 International Conference on Electrical Machines (ICEM)*, 2014, pp. 2114-2119.
39. H. Zahr, J. Gong, E. Semail, and F. Scuiller, "Comparison of Optimized Control Strategies of a High-Speed Traction Machine with Five Phases and Bi-Harmonic Electromotive Force," *Energies*, vol. 9, no. 12, 2016.
40. J. Gong, H. Zahr, E. Semail, M. Trabelsi, B. Aslan, and F. Scuiller, "Design Considerations of Five-Phase Machine With Double p/3p Polarity," *IEEE Transactions on Energy Conversion*, vol. 34, no. 1, pp. 12-24, 2019.
41. G. Dajaku and D. Gerling, "Low costs and high efficiency asynchronous machine with stator cage winding," in *2014 IEEE International Electric Vehicle Conference (IEVC)*, 2014, pp. 1-6.
42. S. Runde, A. Baumgardt, O. Moros, B. Rubey, and D. Gerling, "ISCAD — Design, control and car integration of a 48 volt high performance drive," *CES Transactions on Electrical Machines and Systems*, vol. 3, no. 2, pp. 117-123, 2019.
43. Y. Mini, N. K. Nguyen, and E. Semail, "Sensorless Control for Non-Sinusoidal Five-phase IPMSM Based on Sliding Mode Observer " presented at the SEEDS - Jeunes Chercheurs en Génie Electrique, Oléron, france, Jun, 2019.